Chapter 7

Porous Ceramic Matrix Phase Change Composites for Thermal Control Purposes of Hypersonic Vehicle

Xiangfa Zhou

Additional information is available at the end of the chapter

http://dx.doi.org/10.5772/intechopen.70863

Abstract

Thermal control systems and heat insulation materials are required for a range of hypersonic vehicles ranging from ballistic reentry to hypersonic cruise vehicles, both within Earth's atmosphere and non-Earth atmospheres. The combined thermodynamic/heat transfer relations of the phase change materials (PCMs) in silica nanoporous materials are developed to obtain mass, thickness, and temperature excursion as functions of percentage area of PCM under given maximum energy and thermal flux. The studies show that PCMs are one of the most preferred methods to thermal control applications that can effectively delay or modify the temperature rise of the surface of the aircrafts subjected to high thermal flux. This chapter also introduces the preparations of porous ceramic matrix phase change composite, putting PCMs to use in the internal thermal control materials for the hypersonic vehicles. Porous ceramic matrix serves as the supporting material, which provides structural strength and prevents the leakage of melted PCMs, and PCMs act as thermal absorb material limiting the temperature abruptly rising of the aircrafts. The structural pore properties of the silica matrix with different molar ratios of ethanol (EtOH)/tetraethoxysilane (TEOS) are investigated to determine suitable porous matrices for PCM. To adjust the pore structure of porous silica matrices with different molar ratios of EtOH and TEOS for PCM infiltration is mainly discussed. Furthermore, numerical and experimental studies are proposed to predict and investigate the thermal absorption characteristics of porous silica infiltrated with PCM for thermal control applications.

Keywords: ceramic matrix composite (CMC), phase change materials (PCMs), thermal control systems, preparation, heat transfer modeling

1. Introduction

Controlling the temperature and/or heat transfer is of crucial importance in numerous technical processes and natural occurrences, including cooling of electronics and telecommunications

equipment in aerospace applications. Phase change materials (PCMs), which store excess heat generated from the work components and release it reversibly when needed, provide a smart approach for more efficient temperature management and thermal control utilization. Latent heat absorption phenomena associated with melting of a suitable PCM may be effectively used to delay or modify the temperature rise of the surface subjected to high heat flux. Thermal management utilizing solid-liquid PCMs is one of the most interesting passive thermal management techniques due to its simplicity and reliability. Solid-liquid PCMs including salt hydrates, paraffin waxes, certain hydrocarbons, and metal alloys are often used for thermal protection applications.

Most practical applications for hypersonic vehicles require PCMs to have high density of latent heat and appropriate phase change point. In this criterion, certain hydrocarbons are very promising for temperature controlling applications for its comparative high fusion latent heats, suitable melting temperature, and chemical stability [1]. However, the applications of the kinds of solid-liquid PCMs are largely limited, as leaking of the liquid phase occurs above the phase change point. Thus, accommodation of the PCMs in appropriate host materials is necessary to prevent the leakage of the liquid phase for temperature controlling applications using the solid-liquid phase change. The leakage is usually circumvented by introducing shape stabilization support [2, 3]. Devoting to develop composites with a high PCM load and heat storage density, researchers have been recently interested in silica nanoporous ceramics with high specific area as a shape stabilization matrix or a supporting structure materials as PCMs' skeleton for avoiding leakage of solid-liquid transition [4, 5]. Silica aerogels have been used extensively in many engineering applications. They are sol-gel-derived porous inorganic materials recognized for their low density (as low as 0.01–0.02 g/cm^3) [6], high porosity (>90%) [7], and high specific surface area (600–1000 m^2/g) [8]. These structural properties result in a few thermal conductivities and high optical transparencies [9]. However, monolithic silica aerogels are very fragile and transparent to thermal radiation at high temperature, and these two defects restraint the application range of silica aerogels. Fortunately, researchers have improved both the mechanic strength property and high transparency using reinforced fibers [10] and pacifiers doped in the aerogels [11]. The composite silica aerogels are called silica nanoporous materials, and they have the similar space structure and have superior properties such as higher mechanic strength properties at high temperature [12, 13]. Thus, they have better applicability than the monolithic aerogels. The silica nanoporous materials have broad applications or application prospect in the fields which have strict limit of space or weight, for example, in aeronautics and aerospace [14].

The concept of thermal design using PCM has been well established through various studies in recent decades and is widely used in space applications [15]. To apply PCMs as alternating heat storage and discharge in space applications, the material should accommodate the special needs on the thermophysical properties that include conformance of phase change temperature to the design limits, high latent heat, and low density difference between liquid and solid phases. Structurally and thermally, the synthesis of the support materials for a PCM must be also considered. The supporting materials assure the seepage-proof for the molten PCMs and can withstand some imposed mechanical loads structurally. The supporting materials must be

http://dx.doi.org/10.5772/intechopen.70863

also not degraded the system performance thermally. To design PCM thermal protection system properly, the thermodynamic conservation relations and heat transfer must be considerate.

In this chapter, the combined thermodynamic/heat transfer relations of the PCM in silica nanoporous materials are developed to obtain mass, thickness, and temperature excursion as functions of percentage area of PCM under given maximum energy and thermal flux. And then, the preparation and characterization of form-stable PCM/porous silica ceramic composite are reported. The paraffin acts as thermal absorb material, and porous silica serves as the supporting material, which provides structural strength and prevents the leakage of melted PCM. To adjust the pore structure of porous silica matrices with different molar ratios of EtOH and TEOS for PCM infiltration is mainly discussed. At last, numerical and experimental studies are proposed to predict and investigate the thermal absorption characteristics of porous silica infiltrated with PCM for thermal control applications. The numerical simulation was performed using a volume-averaging technique, and a finite volume modeling (FVM) was used to discretize the heat diffusion equation. The phase change process was modeled using the enthalpy-porosity method.

2. Theory: modeling of combined thermodynamic/heat transfer

To develop the combined thermodynamic/heat mass transfer relations for the PCM/silica nanocomposite, two additional assumptions are made in the development of the relations: firstly, contact resistance between the PCM and the silica nano-materials is assumed negligible, and, secondly, three-dimensional heat transfer effects are neglected, based on the assumption that the skeleton of silica nano-materials is so closely spaced that these effects are negligible.

When the component temperature rise for a particular application exceeds the maximum operational temperature of component, the supporting material raises the equivalent thermal conductivity of the PCM by providing low thermal-resistance paths through the PCM and reduces the temperature gradient necessary to dissipate the imposed cold-plate heat load. The reduction in temperature gradient reduces the temperature excursion of the component. Consider the thermal protection system shown in **Figure 1**. An electrical component is thermally protected by the PCM/silica nanocomposite system. The component internally generates energy cyclically. For cyclical operation, three equations can be derived for the system based on the model.

2.1. Conservation of energy

After the maximum energy that must be stored by the PCM/silica nanocomposite, E_{Max}, is determined, the following heat balance will hold.

$$E_{Max} = \rho_P \cdot A_P \cdot t \cdot h_f + \left[\rho_S \cdot A_S \cdot C_S + \rho_P \cdot A_P \cdot C_P\right] \cdot \frac{t}{2} \cdot (T_{Max} - T) \tag{1}$$

where ρ_P, C_P, and A_P are density, specific heat, and area of PCM, respectively; t is the thickness of the nanocomposite; ρ_S, A_S, and C_S are the density, specific heat, and area of silica, respectively;

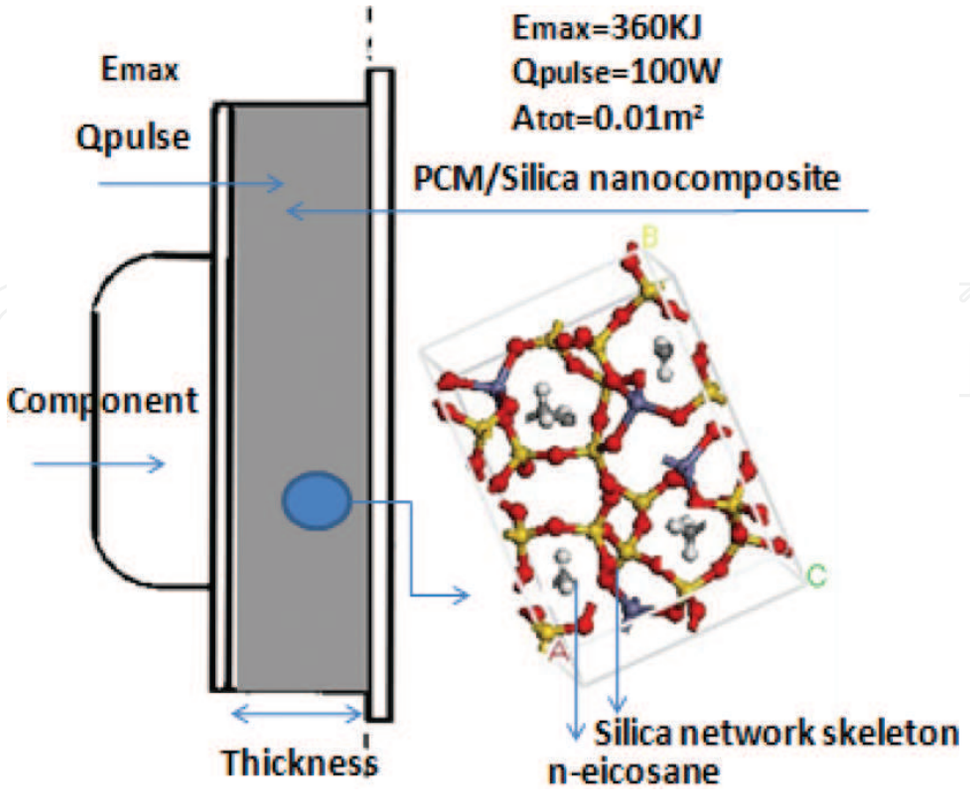

Figure 1. PCM thermal control system and model of PCM/silica nanocomposite.

and $T_{Max} - T$ is the temperature excursion of the component. This equation treats both the energy stored through latent heat of fusion and sensible heat stored within the liquid PCM and the silica nano-materials.

2.2. Conservation of mass

The mass balance shown below will hold:

$$M_{tot} = \left(\rho_P \cdot A_P + \rho_S \cdot A_S\right) \cdot t \tag{2}$$

where M_{tot} is the total mass of the nanocomposite.

2.3. Temperature range constraints

The equation establishes a relation between the total conductivity, K_{tot}; the total area, A_{tot}; the thickness, t; and the temperature excursion $T_{Max} - T$

$$Q_{pulse} = \frac{K_{tot} \cdot A_{tot} \cdot (T_{Max} - T)}{t} \tag{3}$$

2.4. Additive relations

For parallel conductance, the total equivalent conductance can be found from the following equation

http://dx.doi.org/10.5772/intechopen.70863

$$K_{tot} \cdot A_{tot} = k_P \cdot A_P + k_S \cdot A_S \tag{4}$$

This relation neglects three-dimensional effects and contact resistances. The total area is the sum of the cross-sectional areas of the PCM and silica nano-materials.

Thus,

$$A_{tot} = A_P + A_S \tag{5}$$

2.5. Thermodynamic/heat transfer relations

2.5.1. Thermophysical properties

Thermophysical properties are shown in **Table 1**. As shown in **Table 1**, it is concluded that n-eicosane's phase transition at a moderate temperature makes it a candidate phase change materials or PCM which can be used to store thermal energy and control temperature.

2.5.2. Structural and modeling

Silica open-network structure supported by fibers distributed uniformly within. The reinforced silica open-network structure with high porosity and high surface area will benefit for liquid n-eicosane impregnation. The large surface area and low density of porous materials will enhance the shape stabilization capability and thus maximize the surface area per unit volume of PCM. When used in a spacecraft, the materials thermal control system must be small and light. The n-eicosane impregnates in the open network of silica nano-materials as an integrated thermal control system. Among the composite structure, the structural silica nano-materials function not only as reinforced skeleton of the composite but also as heat-conducting materials to transfer heat from the component to the low thermal conductive PCM. The thermal design meets the requirement of total PCM service from alternate melting and freezing during the whole period of mission.

According to this composite structure, the system combining PCM and silica nano-materials is suggested as a new type of thermal control device for the generated heat electronic component.

Name	n-Eicosane ($C_{20}H_{42}$)	Silica nanoporous material
Melting point (°C)	36.7*	—
Latent heat of fusion per unit mass (J/kg × 10^{-3})	247*	—
Specific heat (J/kg K)	2210 at 308 K**	549**
Thermal conductivity (W/m K)	0.15**	0.37**
Density (kg/m^3)	856 at 308 K***	280***

*Measured by DSC.
**Measured by LFA 1000 Laserflash (thermal conductivity/diffusivity).
***Calculated by experiment.

Table 1. Thermophysical properties of n-eicosane and silica nanoporous material.

The PCM thermal control system and the cross section of designed structure, where the PCM is embedded in silica nano-materials, is depicted in **Figure 1**. The cross section of the n-eicosane/silica nanocomposite is an area with 100 mm × 100 mm. The performance of the thermal control device is investigated by numerical analysis. The main purpose of the study is to obtain the functions and relations between the mass, thicknesses, temperature excursion, and percentage area of n-eicosane through combined thermodynamic/heat transfer analysis, which raises the minimum temperature and lowers the maximum temperature. According to the thermal cycle period, composite PCMs accumulate heat and uniformly redistribute it. Thus, the phase change temperature of PCM is the target of temperature control, and it must remain within the maximum/minimum operating temperature range of the electronic component. Furthermore, it must be chemically stable for silica nano-materials, which is the material of PCM support, and there must be a small density difference between solid and liquid phases.

2.5.3. Thermodynamic/heat transfer relations

It is assumed that the component heat is generated periodically according to the system. In detail, there is 3.6×10^2 kJ the maximum energy stored by the PCM/silica nanocomposite, Emax, is determined and then a warming up period of 100 W heating, Q-pulse, during the whole cycle. To obtain a quantitative idea of the functional relationships between the variables described above for a given application, thermodynamic/heat transfer was conducted using the given power and energy requirement, using a given area, and using the thermophysical data of the PCM and silica nano-materials, as described in **Table 1**. These simultaneous Eqs. (1)–(5) can be solved to yield the excursion temperature, T_{Max}-T; the total mass, $M(t)$; and the thickness, t, as functions of PCM area percentage, A_{pcm}/A_{tot}. A MATLAB program was coded to solve the five equations and yields the parametric data discussed above.

The hyperbolic function curve about the relationship between the area percentage of PCM and the excursion temperature, as shown in **Figure 2**, illustrates one interesting fact. The intersections of the curve with the $A_{pcm}/A_{tot} = 0$ vertical line represent the temperature excursion for only a solid silica nano-material heat sink, which means the temperature excursion for a nanocomposite without n-eicosane. The temperature excursion is highest at this condition and decreases drastically with small additions of n-eicosane until a smaller point is reached around 50% n-eicosane. Similarly, the intersections of the curve with the $A_{pcm}/A_{tot} = 1.0$ vertical line represent the temperature excursion for the whole fusion heats of PCM. At this condition, the temperature excursion reaches the smallest value, showing the inferiority of a heat sink of solid silica nano-materials compared to PCM/silica nanocomposite. But the opposite is also true (black curve as shown in **Figure 2**), showing the PCM better controlling ability and repeatability of temperature when intensively change.

The curves about the relationship between the area percentage of PCM and the total mass and thickness, as shown in **Figure 3**, illustrate a monotonic decrease in mass and thickness quantities with addition of PCM. The intersections of the curve with the $A_{pcm}/A_{tot} = 0$ vertical line represent the mass or thickness for only a solid silica nano-materials. The total mass or thickness is most for this condition, and addition of n-eicosane causes a monotonic decrease in both quantities. However, the temperature excursion is highest at this condition when compared to **Figure 2**. Similarly, the intersections of the curve with the $A_{pcm}/A_{tot} = 1.0$ vertical

http://dx.doi.org/10.5772/intechopen.70863

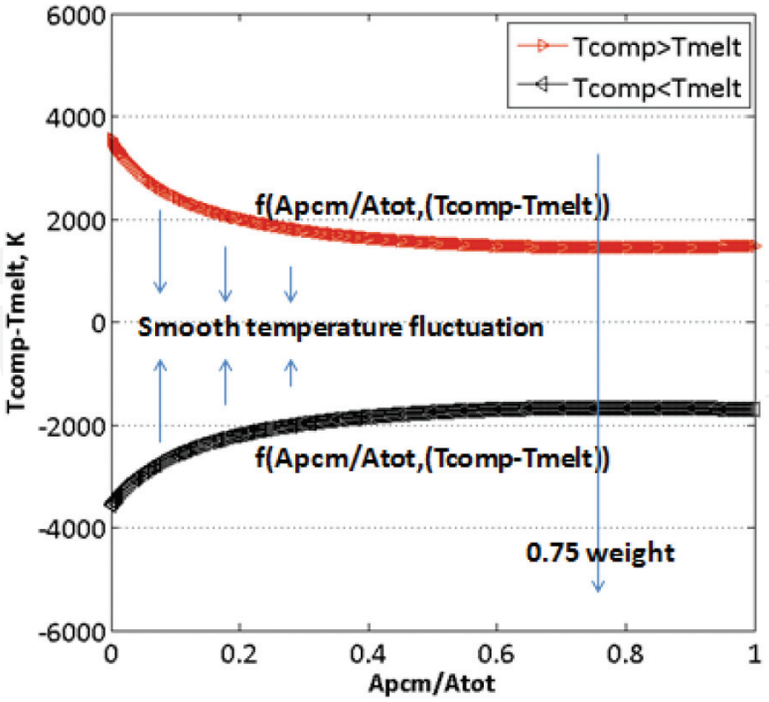

Figure 2. Relationship between the area percentage of PCM and the excursion of temperature.

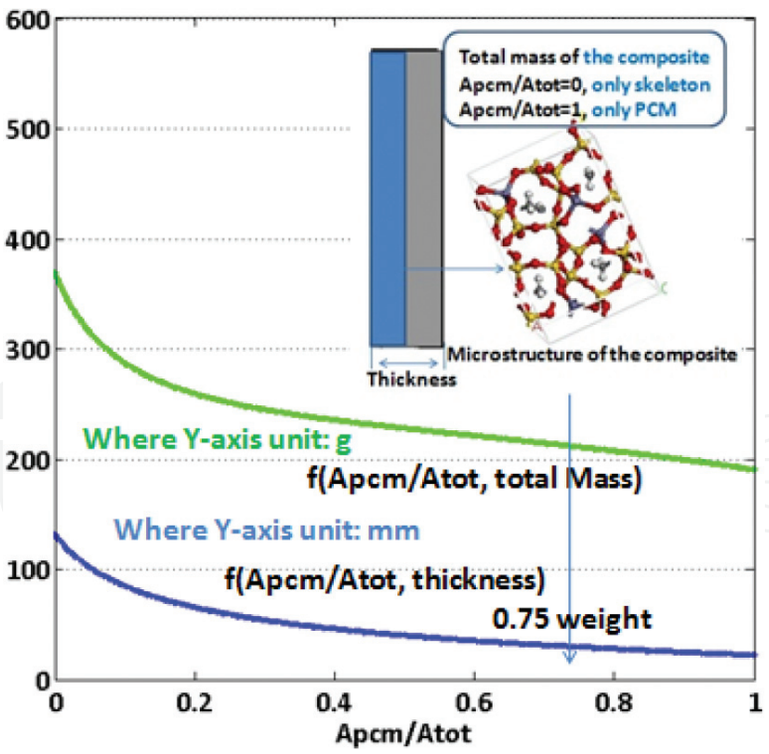

Figure 3. Relationship between the area percentage of PCM and the total mass and thickness.

line represent the mass or thickness for PCM. At this condition, the mass and thickness reach their minimum values, showing also the PCM better controlling the ability of temperature with less mass or volume quantities.

2.6. Enlightening

We performed combined thermodynamic/heat transfer analysis to obtain the total mass, thickness, and temperature excursion as functions of percentage area of PCM under given maximum energy and thermal flux based on the composite structural model and the measured thermophysical data. The relationship between the area percentage of PCM and the excursion temperature is the hyperbolic function, showing the nanocomposite better temperature control management. The relationship between the area percentage of PCM and total mass and thickness shows the nanocomposite better temperature control without much mass or volume quantities. These results are attributed to the strong interaction between the n-eicosane and the silica skeleton, which exhibits novel temperature management and energy utilization.

3. Preparation: characterization and properties of paraffin/porous silica ceramic composites

A form-stable composite of paraffin/porous silica composite was prepared by sol-gel method and melt infiltration. The properties of the composite will be characterized by means of DSC, SEM, and FTIR. Furthermore, the mass fractions of the paraffin in silica matrices prepared by different molar ratios of EtOH/TEOS were recorded to determine the relation between the mass fraction of paraffin and the silica matrices.

3.1. Materials and methods

3.1.1. PCM

The technical grade paraffin (n-eicosane: the chemical formula $C_{20}H_{42}$) used in this study was supplied by Nanyang Chemicals Company in China. Thermophysical data of the PCM are given in **Table 1**. The melting temperature ranges, and fusion heats of the PCMs were measured by a DSC instrument (NETZSCH STA449C) with heating rate at 10°C/min in the temperature range of 20–80°C.

3.1.2. Preparation of n-eicosane/silica nanocomposite

The preparation process of n-eicosane/silica nanoporous composite is shown in **Figure 4**. Firstly, the support materials—porous silica for the PCM—were synthesized by a two-step sol-gel process. Secondly, reinforced fibers (main compositions: $SiO_2 > 99.95\%$) were exploited as structural reinforcement matrix.

The fibrous materials were uniformly pre-shaped in a mold and sol-gel mixtures and closely infiltrated the fibers by pouring them into the mold. Then, the mold includes silica sol-gel mixtures with fiber material uniformly distributed within which were supercritically dried in an autoclave above the critical temperature and critical pressure after gelation and aging in ethanol. The illustration of supercritical fluid drying equipment is shown in **Figure 4**. The final bulk silica nanoporous materials are obtained.

http://dx.doi.org/10.5772/intechopen.70863

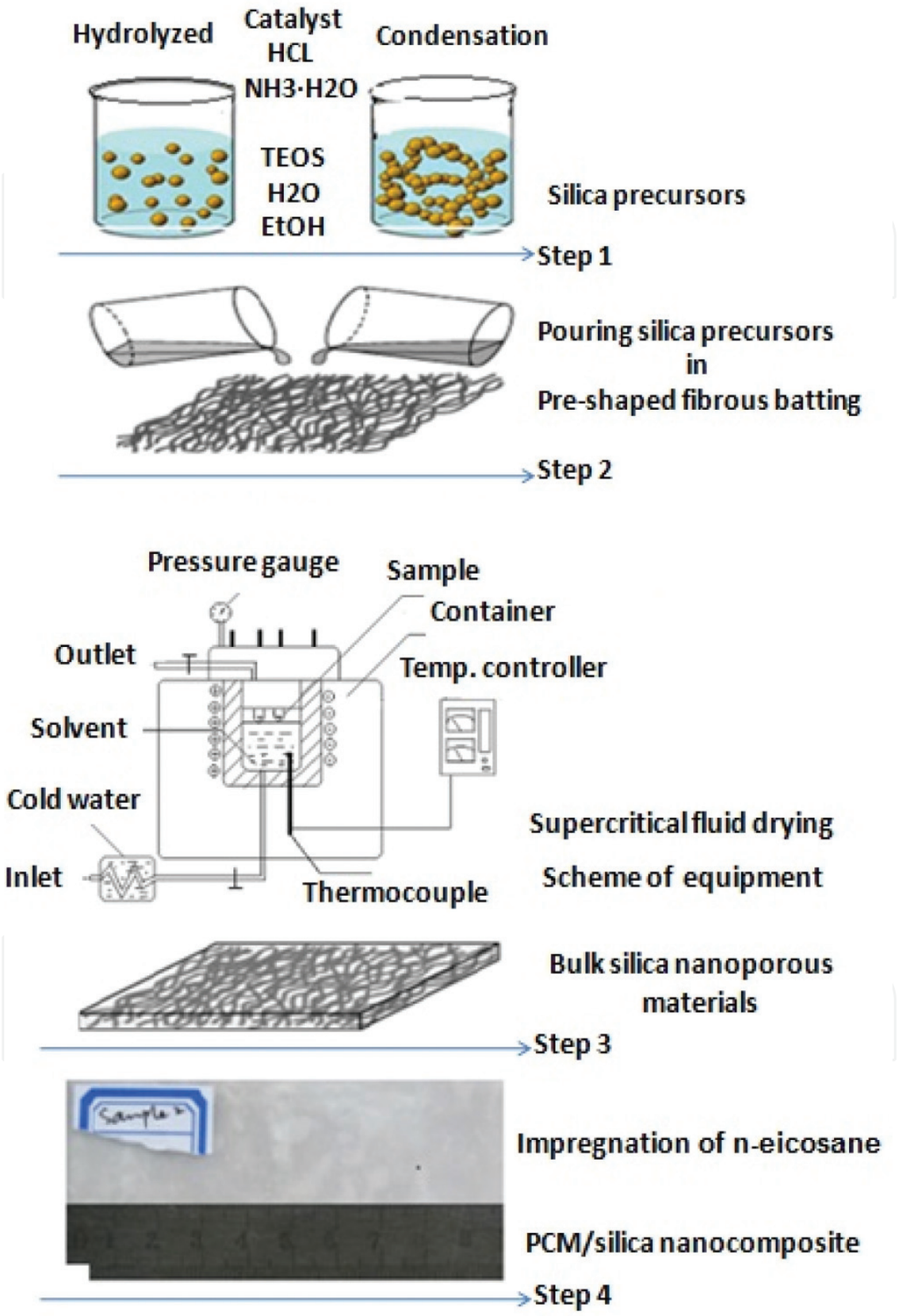

Figure 4. Experimental preparation process of n-eicosane/silica nano-composite.

3.1.3. Pore structure modification of silica matrix infiltrated with paraffin

The molar ratios of EtOH and TEOS were designed as the reactants to prepare the porous silica. The final silica showed a different pore structure with the change of EtOH/TEOS. The mass fraction of the melted paraffin infiltrated into the porous silica was closely related to the pore structure of silica. The mass fractions of the paraffin in silica matrices prepared by different molar ratios of EtOH/TEOS were recorded to determine the relation between the mass fraction of paraffin and the silica matrices.

3.2. Characterization and properties

3.2.1. Pore structure modification of porous silica matrices

The adsorption-desorption measurements were performed by ASAP 2000 micromeritic apparatus. Analysis of the surface areas of the porous silica samples was conducted by Brunauer-Emmett-Teller (BET) method [16]. The method also determines the external/mesoporous surface area and extends the analysis of adsorbed gas from the lower P/P_0 range of Langmuir monolayer and BET multilayer adsorption to the higher P/P_0 range. The pore size is also determined using the Barrett-Joyner-Halenda (BJH) method [17, 18].

The N_2 adsorption-desorption isotherms of the silica samples are given in **Figure 5**. It shows that the sorption isotherms of the samples with the moral ratios of the EtOH/TEOS (E) = 2, E = 3, and E = 5 belong to Type IV mesoporous structures according to IUPC classification, nitrogen absorption of which was linearly increased with the relative pressure until 0.92 and then increased abruptly and saturated at near saturated pressure during absorption process. During desorption, nitrogen was dissociated, and the cumulative absorbed volume decreased greatly in the region of 0.90–0.95. For E = 10 porous silica, the region of great desorption change shifted to 0.97–1. It was shifted to higher region for E = 20 porous silica, and the steep slopes may be associated with capillary condensation in larger pores (>50 nm) and classified as Type II according to the Kelvin equation and IUPC classification. N_2 sorption data indicates that the E = 2, E = 3, and E = 5 silica are comprised of small-sized pores compared to those of

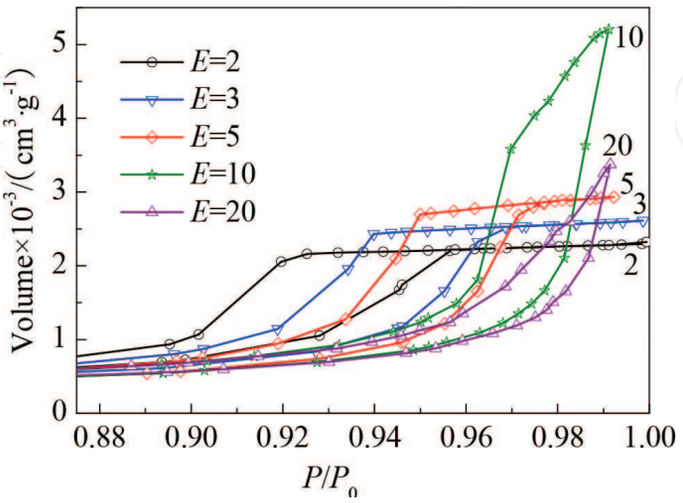

Figure 5. The N_2 adsorption-desorption isotherms of the silica samples.

the E = 10 and E = 20 silica. Pore structural characteristics of the samples obtained from the analysis of N_2 sorption data were shown in **Table 2**.

Figure 6 shows the pore size distributions of samples with different molar ratios of EtOH/TEOS measured by nitrogen desorption method (BJH method). The network formations of silica are known to be affected by water/Si, catalyst, pH, temperature, and ethanol/Si [19]. Results show that the EtOH/TEOS molar ratio causes the difference of silica network structures because the greater ethanol content retards the gelation time and results in the network structures with larger pores when the other basic compositions hold constant.

Microphotographs are taken from the fracture surface of the silica samples using JSM-6360LV scanning electron microscope. SEM of the microstructures of samples with the three kinds of EtOH/TEOS molar ratios of 2, 10, and 20 is given in **Figure 7**. The pore size increases when the molar ratios of the EtOH/TEOS increase by comparing with the samples with the three kinds of molar ratios of the EtOH/TEOS; the pore size of the sample with the EtOH/TEOS molar ratio of 20 is bigger than the other two types of the EtOH/TEOS molar ratios of 2 and 10. Several

EtOH/TEOS	Smulti ($m^2 \cdot g^{-1}$)	Ssingl ($m^2 \cdot g^{-1}$)	C	V ($cm^3 \cdot g^{-1}$)	Davera (nm)	DBJH (nm)
2	618.3	583	44.31	3.594	23.3	23.4
3	624.8	577.7	88.42	4.042	25.9	32.4
5	565.4	518.9	83.86	4.534	32.1	38.5
10	606.5	552.8	94.22	8.051	53.1	59.5
20	596.7	573	91.55	5.219	56	60.7

Note: Smulti, multiple point BET values; Ssingl, mono-point BET values; V, pore volume; Davera, mean pore diameter; DBJH, pore diameter by BJH method.

Table 2. Pore characteristics of the samples with various molar ratios of EtOH/TEOS (E) obtained from the analysis of N_2 sorption data.

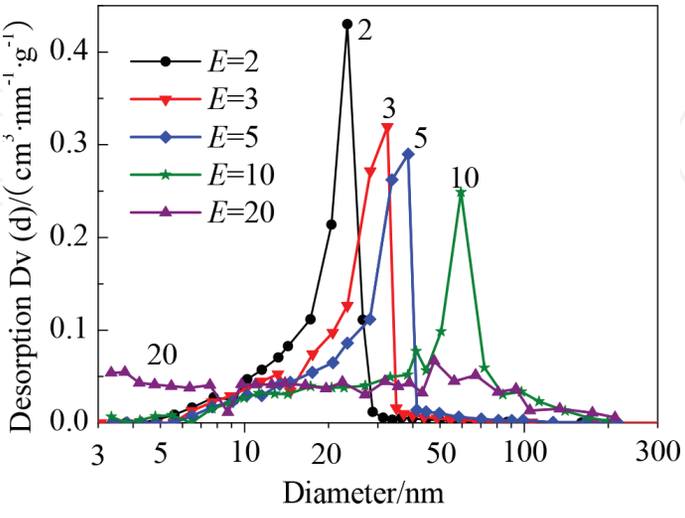

Figure 6. The pore size distributions of samples with different molar ratios of EtOH/TEOS measured by nitrogen desorption method (BET).

kinds of form-stable paraffin/porous silica composites were successfully prepared in our recent study. Using the silica matrices synthesized from the EtOH/TEOS ratio of 10, the PCM showed better thermal absorption characteristics, which is suitable for the fields of requiring cooling at high temperatures such as aircraft electronics and spacecraft devices.

3.2.2. The mass fractions of the paraffin

The relation between the mass fraction of the paraffin infiltrated the three kinds of molar ratios of EtOH/TEOS (E = 2, E = 10, E = 20) silica matrices and the infiltration time was plotted in **Figure 8**. The mass fraction of the paraffin in porous silica increases with the infiltration time, and the E = 10 and E = 20 silica matrix composites reached to 75% at 180 s, while E = 2 silica matrix composite reached to 68%, and then they all increase a little with further time. It indicates that the maximum mass fractions of the paraffin as PCM in E = 10 and E = 20 silica matrices are over than one of the E = 2 silica matrices and the bigger mass fraction of the

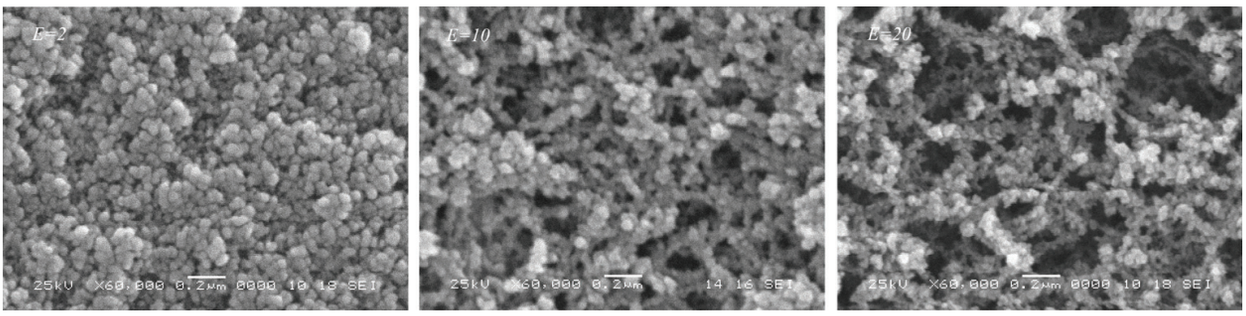

Figure 7. SEM of the microstructures of samples with the three kinds of EtOH/TEOS molar ratios of 2, 10, and 20.

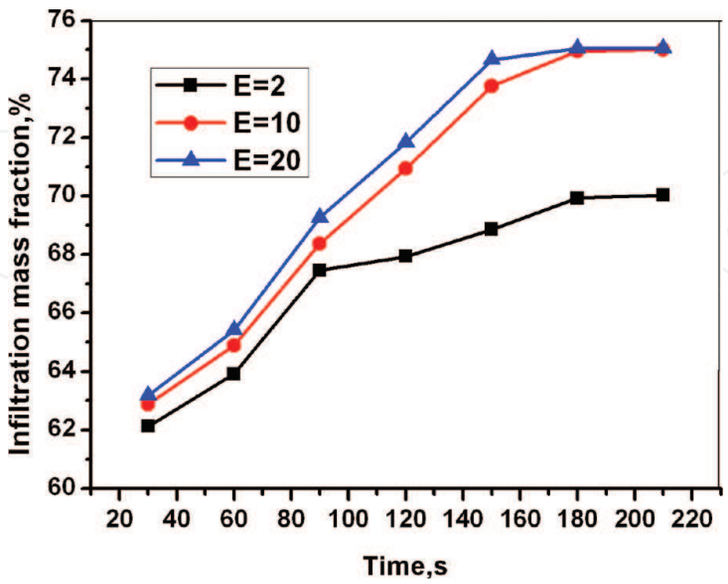

Figure 8. The relation between the mass fractions of the paraffin infiltrated the three kinds of molar ratios of EtOH/TEOS (E = 2, E = 10, E = 20) silica matrices and the infiltration time.

paraffin meant considerable latent heat energy storage potential. The pore size of porous silica becomes larger with the increase of the EtOH/TEOS molar ratios; when the molar ratios of EtOH/TEOS are 10 and 20, the average pore size of the synthesized silica are 53.1 and 56.0 nm, respectively. The maximum mass percentage of paraffin as PCM in the E = 10 and E = 20 silica matrices reached to 75 wt% and over than those of the E = 2 silica matrix. When the molar ratios of EtOH/TEOS are 10 and 20, the synthesized silica matrices are suitable to serve as supporting materials of the PCM.

3.2.3. Structure analysis

The morphologies of silica nanoporous materials and PCM/silica composite were observed with a field emission scanning electron microscope (FE-SEM: JSM-6700F, JEOL, Japan, with a thin Pt-Pd coating). **Figure 9** compares the SEM of the microstructures of porous silica and the composite. The microstructure of the porous silica (**Figure 9a**) is porous and connected each other, while the microstructure of the composite (**Figure 9b**) shows that the paraffin was dispersed uniformly into the porous network of silica ceramics, which used as supporting material and provided a mechanical strength to the PCM. The maximum mass fraction of paraffin dispersed into the composites was measured as 75%, and there was no leakage of the paraffin from the surface of the composite up to this mass fraction even over its melting temperature.

3.2.4. Chemical properties

FTIR spectra of the paraffin and the silica and the paraffin/porous silica composite are shown in **Figure 10**. In FTIR spectra of the paraffin, the peaks at the wave numbers of 2935 and 2860 cm^{-1} are caused by stretching vibration of C–H, peaks at around 1500 cm^{-1} belong to the deformation vibration of $–CH_2$ and $–CH_3$, and the peak at 750 cm^{-1} represents the rocking vibration of $–CH_2$. In FTIR spectra of the silica, the peaks at 1012 and 810 cm^{-1} are caused by bending vibration of Si–O, and an intense band at the wave number of 1090 cm^{-1} is typical of

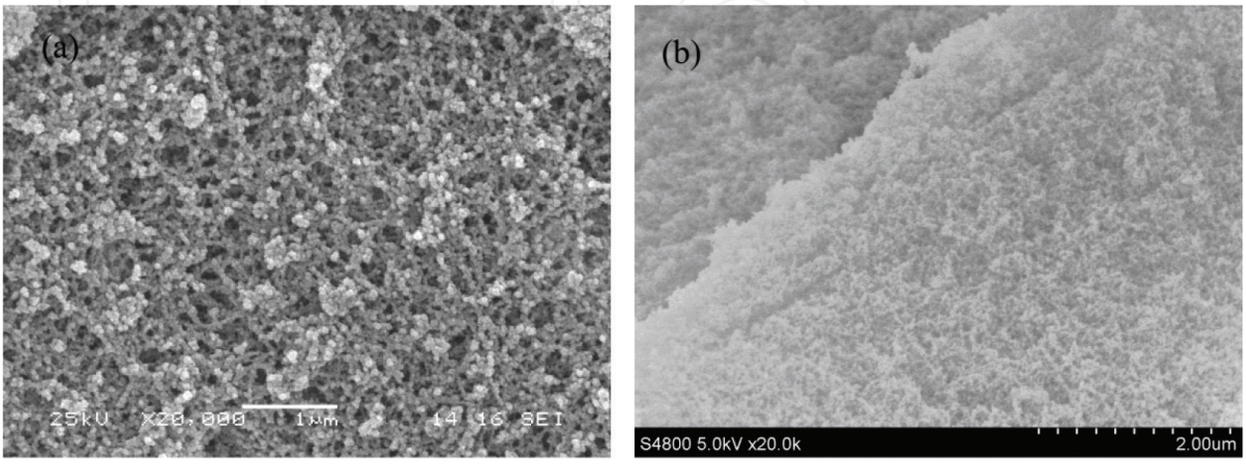

Figure 9. The SEM of the microstructures of porous silica (a) and the PCM/nano-composite (b).

the bending vibration of Si–O. And, the peak at 3449 cm^{-1} represents the stretching vibration of functional group of Si–OH. For the composite, the peaks at the wave numbers of 3500, 2935, 2860, 1500, 1090, and 750 cm^{-1} have corresponding vibration, and no significant new peaks were observed. The FTIR spectra illustrate that the composite is just a physical combination of silica ceramics and paraffin.

3.2.5. Thermal properties

The DSC curves of the paraffin and the composite are shown in **Figure 11**. From **Figure 1a**, the latent heat of the paraffin is 182.22 kJ/kg (T_m = 56.8°C). TG curve shows that weight of paraffin hardly changes, which indicates the paraffin used as PCM has good thermal chemical stability. **Figure 11b** indicates that heat storage capacity of the composite happened at melting point

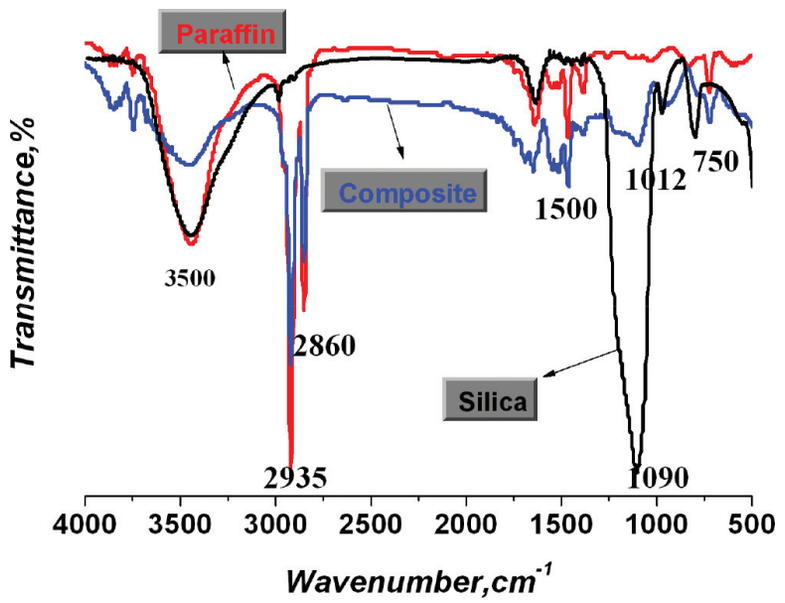

Figure 10. FTIR spectra of the paraffin and the silica and the paraffin/porous silica composite.

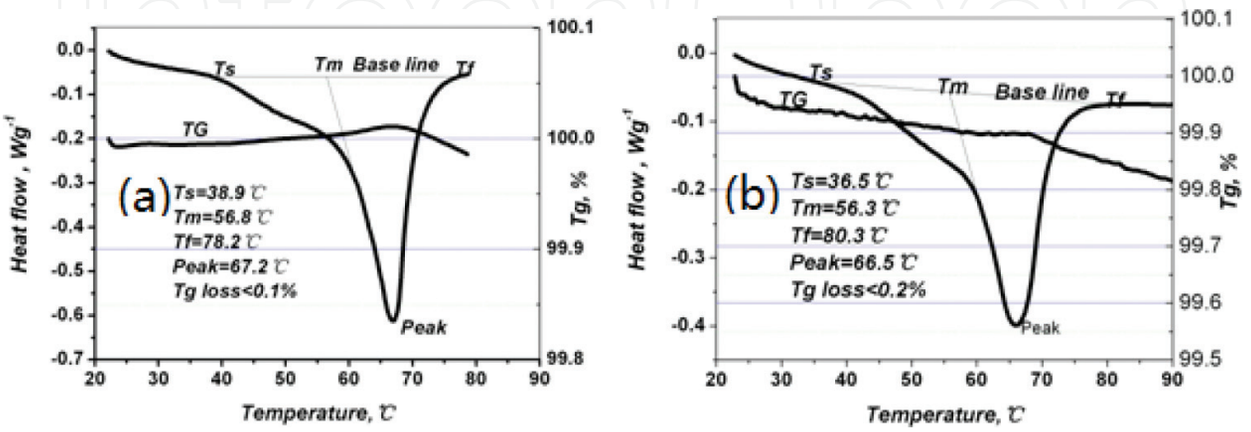

Figure 11. The DSC-TG curves of the paraffin (a) and the PCM/silica composite (b).

56.3°C is 165.16 kJ/kg. TG curve indicates that weight of the composite changes very a few; weight loss of the composite is less than 0.2%.

4. Applications: thermal protection purposes

Numerical and experimental studies are proposed to predict and investigate the thermal absorption characteristics of porous silica infiltrated with PCM for thermal protection applications. The numerical simulation was performed using a volume-averaging technique, and a finite volume modeling (FVM) was used to discretize the heat diffusion equation. The phase change process was modeled using the enthalpy-porosity method.

4.1. Experimental procedure

Three porous silica cylindrical disks (100 mm in diameter and 10 mm thick) with the three different solid-liquid PCMs (two kinds of paraffin and one kind of xylitol) were fabricated as the solid matrices of the silica-PCM composites according to our recent study. The thermophysical data for these samples are given in **Table 3**.

The composites (100 mm in diameter and 10 mm thick) were then introduced into the experimental setup (see **Figure 12** left). The temperature was recorded as it varied with time. The top and bottom walls of the container were insulated by adiabatic materials. For the sake of validation of the numerical model and assumptions, the temperature of the cold face of composite X98$^{\#}$ as a function of time was deduced by the numerical simulation.

4.2. Numerical model

A schematic diagram of the composite and two-dimensional grids is given in **Figure 12**. (Sample dimensions: 180 mm in diameter and 120 mm thick). Due to the symmetry and regularity, the samples were formulated with two-dimensional axissymmetric coordinates

	C58$^{\#}$	**C64$^{\#}$**	**X98$^{\#}$**
Sample volume (m^3)	3.05E−3	3.05E−3	3.05E−3
Mass before infiltration (kg)	7.20E−1	7.20E−1	7.20E−1
Mass after infiltration (kg)	2.79	2.83	4.16
PCM (paraffin or xylitol) mass rate (%)	74.19	74.56	82.69
Phase change point (K)	324	329	363
Heat storage capacities $(kJ(kg)^{-1})$	172	165	198
Density (kgm^{-3})	914.75	927.87	1363.93
Thermal conductivity $(Wm^{-1}\,K^{-1})$	0.38	0.38	0.46
Specific heat $(kJ(kg)^{-1}\,K^{-1})$	2.4	2.4	3.8

Table 3. Properties of the porous silica matrix composites.

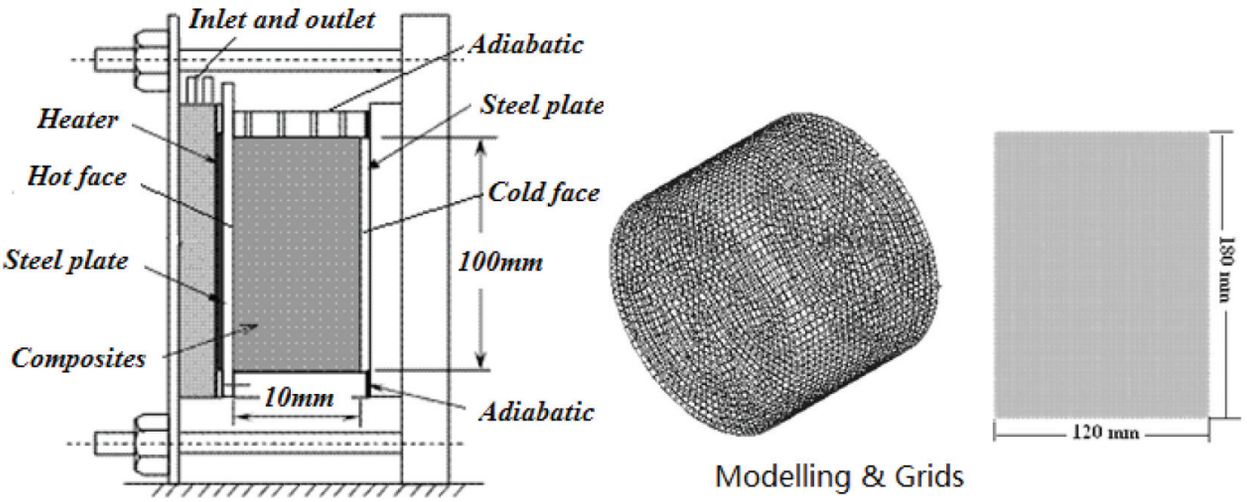

Figure 12. Experimental setup for heat transfer of phase change composite (100 mm in diameter and 10 mm thick) and modeling and grids for the composite (180 mm in diameter and 120 mm thick).

and uniformly split quadrangle grids in all 19,481 nodes by Gambit 2.2.30, and the boundary conditions were specified.

4.2.1. Assumptions and governing equations

The two-dimensional governing equations have been made based on the following assumptions:

The thermophysical properties are different for the solid and liquid phases but are dependent of temperature.

Heat loss from the container to its surroundings is negligibly small.

Based on these assumptions, the enthalpy-porosity method [20] was used for the phase change region in the PCM.

Continuity:

$$\frac{\partial \rho}{\partial t} + \frac{\partial (\rho u)}{\partial x} + \frac{\partial (\rho v)}{\partial y} = 0 \tag{6}$$

where ρ is the density, u is the velocity in u direction, t is the time, and v is the velocity in v direction.

u-Momentum:

$$\rho\left(\frac{\partial u}{\partial t} + u\frac{\partial u}{\partial x} + v\frac{\partial u}{\partial y}\right) = \mu\left(\frac{\partial^2 u}{\partial x^2} + \frac{\partial^2 u}{\partial y^2}\right) - \frac{\partial p}{\partial x} + S_u \tag{7}$$

v–Momentum:

$$\rho\left(\frac{\partial v}{\partial t}+u\frac{\partial v}{\partial x}+v\frac{\partial v}{\partial y}\right)=\mu\left(\frac{\partial^2 v}{\partial x^2}+\frac{\partial^2 v}{\partial y^2}\right)-\frac{\partial p}{\partial y}+S_v \tag{8}$$

Energy:

$$\rho\left(\frac{\partial H}{\partial t}+u\frac{\partial H}{\partial x}+v\frac{\partial H}{\partial y}\right)=\frac{k}{c_p}\left(\frac{\partial^2 H}{\partial x^2}+\frac{\partial^2 H}{\partial y^2}\right)+S_k \tag{9}$$

where the source term is $S_h=\frac{\rho}{c_p}\frac{\partial(\Delta H)}{\partial t}$, and

$$\begin{aligned} H&=h+\Delta H\\ h&=h_{ref}+\int_{T_{ref}}^{T}c_p dT\end{aligned} \tag{10}$$

where H is the enthalpy, T is the temperature, and ΔH is the specific enthalpy.

The density and dynamic viscosity of the liquid PCM depend on its temperature [20, 21].

Boundary conditions

Given the constant temperature of the cold face and the adiabatic top and bottom wall,

$$\begin{aligned} T(x,y,t)|_{x=d}&=T_{cold}\\ \frac{\partial T}{\partial y}|_{y=0,\,t}&=0\end{aligned} \tag{11}$$

Initial conditions

Assuming initial temperature conformity and a fixed temperature of the hot face,

$$\begin{aligned} T(x,y,t)|_{t=0}&=T\\ T(x,y,t)|_{x=0,\,t>0}&=T_{hot}\end{aligned} \tag{12}$$

The numerical solution was carried out using the Fluent 6.3 software package [19]. The number of computational grids was ~19,200 for the 2D model after grid-independent tests. The time step in the simulations was as small as Δt = 0.1 s. The convergence was also checked at each time step, with convergence criteria of 10^{-4} for velocity components and 10^{-7} for energy equation.

4.3. Experimental results and discussion

The composites had different thermophysical data owing to the three types of organic PCMs used during the preparation of the porous silica-PCM composites (see **Figure 4** and **Table 3**). The varying heat storage capacities of the composites have an influence on the experimental

melting process. Experiments are required to determine the suitable silica-PCM for the service conditions.

The thermal protection properties of the three types of porous silica-PCM were experimentally studied (**Figure 13**). **Figure 13a** compares the temperature of the cold face of the composites when they are subjected to same hot face temperature; **Figure 13b** represents that their temperature of cold face varies with time as they are subjected to hot face temperature (600°C). As can be seen in the figure, the X98# composite shows the best heat absorption properties among the three composites. On the one hand, the temperature of the cold face of the composite X98# is 45°C, while one of the other two composites is 75°C as the three types of composites subjected to same hot face temperature (400°C) (see **Figure 13a**). On the other hand, the slope of the time-temperature curve of the X98# composite decreases at a temperature ~ 80–90°C, which is close to the phase transition range of the X98# composite and does not vary substantially with time. This trend is obvious at the melting temperature of the X98# composite, and it did not appear for the other two composites 58# and C64#, as they are above their phase change temperature and had already melted (see **Figure 13b**). For the cold face of composite X98#, good agreement is obtained when comparing the temperature as a function of time to the numerical simulation results (**Figure 13b**).

4.4. Results and discussion

Numerical studies have been carried out for the three types of composites under identical conditions. The temperature contours for the composite C58# at a constant hot face temperature (573 K), and different time intervals (10, 30, and 60s) are shown in **Figure 14**. The temperature rises quickly at the beginning of the heating process and propagated as time goes on, as the melting of the composites started at the hot face in direct contact with the heating surface and the solid-liquid interface moved gradually in the axial direction over time. For the composite C64#, the heat transfer numerical studies showed the same melting process

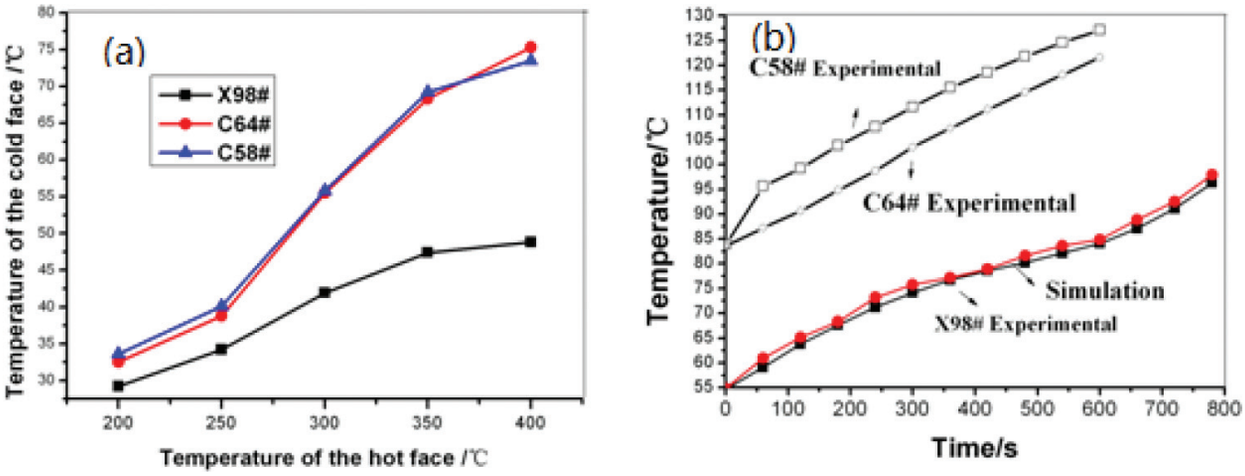

Figure 13. (a) Comparison of cold face and hot face temperature of three types of composites. (b) Cold face temperature varied with time as hot face temperature is 600°C.

http://dx.doi.org/10.5772/intechopen.70863

compared with the composite C58#. For the composite X98#, the temperature contours at different time intervals (10, 30, 60, and 120 s) are shown in **Figure 15** under identical conditions (a constant hot face temperature (573 K)), and liquid fraction contours of the composites X98# at 180 s are shown in **Figure 16**, which indicated the more stable thermal performance during

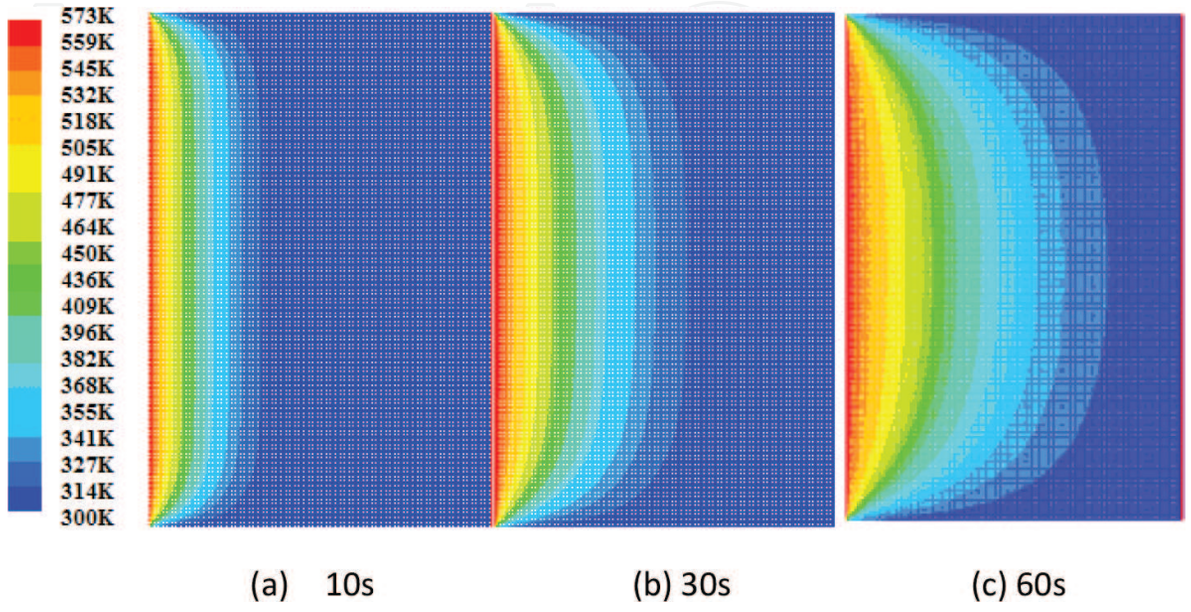

Figure 14. Contours of temperature of the composite C58# (time intervals = (a) 10s, (b) 30s, (c) 60s).

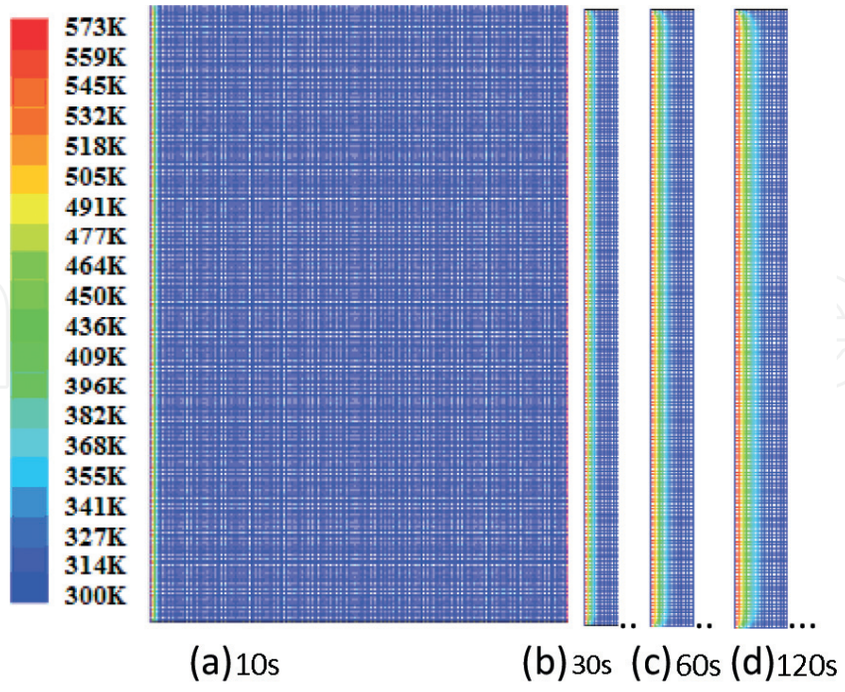

Figure 15. Contours of temperature of the composite 98# (time intervals = (a) 10s, (b) 30s, (c) 60s, (d) 120 s) (left).

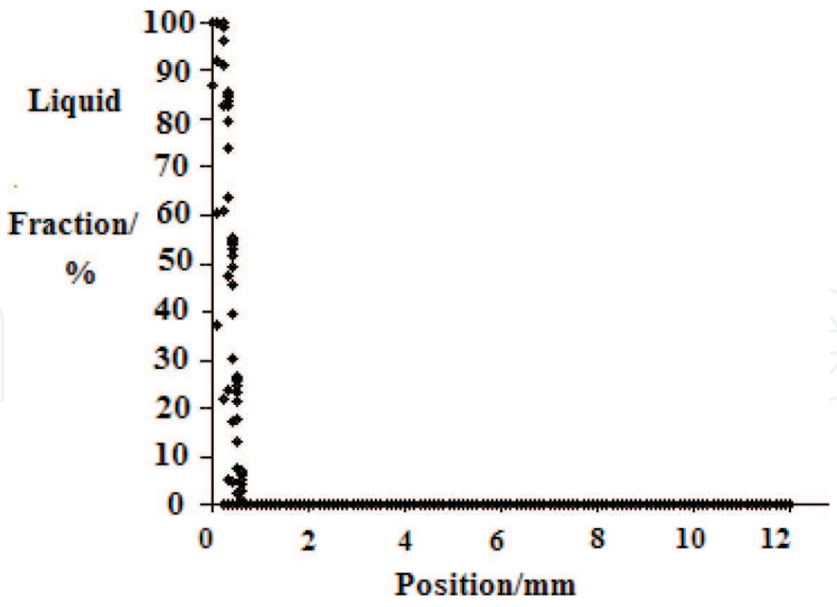

Figure 16. Liquid fraction of the composite 98# at 180 s (right).

the melting process due to higher heat storage capacities and phase change point as compared with the composites C58# and C64#.

The experimental results indicated that the suitable silica-PCM for the service conditions is the composite X98#. In addition, the composite X98# showed the more stable thermal performance during the melting process based on numerical results for the temperature and liquid contours of the composites. From the thermophysical data of the porous silica matrix composites (**Table 3**), the mass infiltration rate of PCM (xylitol) in the porous silica matrix composite X98# is more than the other two composites C58# and C64#. The X98#-type composite has both high heat storage capacity and a high phase change point. Thus, it may be concluded that controlling the surface temperature depends mainly on these two main parameters.

4.5. Conclusions

The effects of the heat storage capacity and thermal properties of porous silica filled with different PCMs were studied numerically and experimentally. The results indicate that the heat storage capacity and phase change point of the composites play important roles in their thermal performance. It has been illustrated that a higher heat storage capacity leads to more stability in the thermal performance of the composite and the phase change point of the composite determined its service conditions.

Acknowledgements

This project is funded by the China Scholarship Council (CSC). The author would like to acknowledge the American Association for the Advancement of Science and Nano Technology and New Materials Institute of Changsha University in China.

Author details

Xiangfa Zhou

Address all correspondence to: flucky-zhou@163.net

Institute of Nano-Technology and New Materials, Changsha University, Hunan, China

References

[1] Dincer I, Rosen MA. Thermal Energy Storage Systems and Applications. England: Wiley; 2002

[2] Su JC, Liu PS. A novel solid-solid phase change heat storage material with polyurethane block copolymer structure. Energy Conversion and Management. 2006;**47**(18–19):3185-3191

[3] Jiang Y, Ding EY, Li GK. Study on transition characteristics of PEG/CDA solid–solid phase change materials. Polymer. 2002;**43**(1):117-120

[4] Grandi S, Magistris A, Mustarelli P, Quartarone E, Tomasi C, Meda L. Synthesis and characterization of SiO_2-PEG hybrid materials. Journal of Non-Crystalline Solids. 2006;**352**(3):273-280

[5] Wang W, Wang CY, Li W, Fan XX, Wu ZH, Zheng J, Li XG. Novel phase change behavior of n-eicosane in nanoporous silica: Emulsion template preparation and structure characterization using small angle X-ray scattering. Physical Chemistry. 2013;**15**(34):14390-14395

[6] Tabata M, Adachi I, Ishii Y, Kawai H, Sumiyoshi T, Yokogawa H. Development of transparent silica aerogel over a wide range of densities. Nuclear Instruments and Methods A. 2010;**623**(1):339-341

[7] Wagh PB, Ingale SV, Gupta SC. Comparison of hydrophobicity studies of silica aerogels using contact angle measurements with water drop method and adsorbed water content measurements made by Karl Fischer's titration method. Journal of Sol-Gel Science and Technology. 2010;**55**(1):73−78

[8] Reynolds JG, Coronado PR, Hrubesh LW. Hydrophobic aerogels for oil-spill cleanup—Intrinsic absorbing properties. Energy Sources. 2001;**23**(9):831−843

[9] Husing N, Schubert U. Aerogels airy materials: Chemistry, structure, and properties. Angewandte Chemie, International Edition. 1998;**37**(1–2):23-45

[10] Zhang ZH, Shen J, Ni XY, Wu GM, Zhou B, Yang MX, Gu XH, Qian MJ, Wu YH. Hydrophobic silica aerogels strengthened with nonwoven fibers. Journal of Macromolecular Science, Part A. 2006;**43**(11):1663-1670

[11] Harel E, Granwehr J, Juliette A. Seeley Alex Pines. Multiphase imaging of gas flow in a nanoporous material remote-detection NMR. Nature Materials. 2006;**5**:321

[12] Morris CA, Anderson ML, Stroud RM, Merzbacher CI, Rolison DR. Silica sol as a nanoglue: Flexible synthesis of composite aerogels. Science. 1999;**284**:622-624

[13] Bi C, Tang GH, Hu ZJ, Yang HL, Li JN. Coupling model for heat transfer between solid and gas phases in aerogel and experimental investigation. International Journal of Heat and Mass Transfer. 2014;**79**:126-136

[14] Kim TY, Hyun BS, Lee JJ and Rhee J. Numerical study of the spacecraft thermal control hardware combining solid-liquid phase change material and a heat pipe. Aerosp Sci Technol, 2013;**27**(1):10-16

[15] Pal D, Joshi YK. Thermal management of an avionics module using solid-liquid phase-change materials. Journal of Thermophysics and Heat Transfer. 1998;**12**(2):256-262

[16] Gregg SG, Sing KSW. Adsorption Surface Area and Porosity. New York: Academic Press; 1982. p. 236-238

[17] Barrett EP, Joyner LG, Halenda P. The determination of pore volume and area distributions in porous substances: Computations from nitrogen isotherms. Journal of the American Chemical Society. 1951;**73**:373-380

[18] Sing KSW, Everett DH, Haul RAW. Reporting physic sorption data for gas/solid systems with special reference to the determination of surface area and porosity. Pure and Applied Chemistry. 1985;**57**:603

[19] Venkateswara Rao A, Sharad DB. Synthesis and physical properties of TEOS-based silica aerogels prepared by two step (acid-base) sol-gel process. Solid State Sciences. 2004;**6**: 945-952

[20] http://www.fluent.com

[21] Reid RC, Prausnitz JM, Poling BE. The Properties of Gases and Liquids. New York: McGraw-Hill; 1987. p. 439-456